Cation Disorder in Cu_2ZnSnS_4 Thin Films: Effect on Solar Cell Performances

Claudia Malerba, Matteo Valentini, and Alberto Mittiga*

High (300 °C) and low (160 °C) temperature post deposition annealing treatments are performed on Cu_2ZnSnS_4 (CZTS) thin film solar cells to modify the order degree of the CZTS absorber and investigate its effect on the device performances. Large and reversible changes of solar cell parameters are observed, with photovoltaic conversion efficiencies varying from about 4% in the case of more ordered materials, up to nearly 8% after the disordering treatment. Both spectrophotometry and photoluminescence reveal that the ordered materials are characterized by a higher bandgap and a lower deep defect density, whereas the absorption tails and the red shift of the luminescence peak compared to the bandgap are found to be independent of the ordering level. Coherently with the bandgap variation, solar cells in the ordered state are characterized by a lower short circuit current density and a higher open circuit voltage. Ordered devices are found to be limited by low fill factor values, often associated with anomalous "S-shaped" light *J–V* curves revealing a blocking behavior. A mechanism based on the increase of a blocking barrier at the CZTS/MoS_2 back interface induced by a change in the valence band offset is proposed to explain the lower performances of the ordered devices.

1. Introduction

Kesterite semiconductor $Cu_2ZnSn(S,Se)_4$ attracted much attention in recent years due to its high absorption coefficient in the visible energy range and the high abundance of the constituent elements, which make this material a potential absorber to replace chalcopyrite $Cu(In,Ga)S_2$ (CIGS) in thin film solar cells. However, the reported record efficiency of 12.7% of CZTSSe-based devices are still far from their theoretical limits (≈30%).[1,2] The pure sulfide compound Cu_2ZnSnS_4, containing only more-abundant sulfur and showing higher bandgap E_g (1.45–1.65 eV) than its selenide CZTSe counterpart (0.95–1.05 eV) is even more attractive, being a good candidate for tandem top cell application.[3,4] However, slightly lower performances have been reported for single-heterojunction devices based on pure sulfide CZTS, with a record efficiency of 9.2%.[5,6] The main limiting factor has been identified in the large open-circuit voltage deficit ($E_g/q–V_{oc}$), which can be imputed to interfacial recombination caused by not-optimal band alignment between CZTS absorber and CdS buffer, large absorption tails due to defects-induced electrostatic potential or bandgap fluctuations and low minority carrier lifetime.[7–10]

Recently, a beneficial effect of post deposition annealing (PDA) treatments on kesterite thin film solar cells (SCs) has been reported in several works.[11–14] The physical mechanisms behind this improvement are not yet completely understood and a large scattering in the optimum conditions for the PDA process (temperature, time, atmosphere) is also found among the different research groups. A significant efficiency increase has been achieved with PDA treatments either of the bare absorber (before the buffer deposition), or of the buffer/absorber bilayer or of complete devices.[11–16]

For example, efficiencies over 10% are obtained by the IBM group with a 10 min thermal annealing of the bare CZTSSe at 375 °C in air. The positive effect on the cell efficiency is attributed by the authors to the formation of a copper poor surface and to the grain boundaries passivation by SnO_x.[11]

Similar results are reported in the work by Xie et al., in which the best results are obtained using a 1 h thermal annealing in air at 400 °C of the CZTSSe before the CdS deposition.[12] Surprisingly, in the same work a similar annealing performed at 200 °C gives shunted devices with nearly zero efficiency. The annealing performed in N_2 leads to results similar to those obtained in air and the variations of device performances are therefore imputed to a change in the sodium distribution along the cell thickness, rather than to oxidation effects. Different results are reported by Neuschitzer et al. for CZTSe deposited on Mo covered by a 10 nm thin ZnO film, since not-working devices are obtained with the annealing in air of the bare absorber whereas the same process performed in argon results in devices with 5% efficiency.[13] In the same work, best results are instead obtained on complete device thermally annealed at 200 °C in air for 35 min, reaching efficiencies of up to 8.3%. The device

Dr. C. Malerba, Dr. M. Valentini, A. Mittiga
ENEA Casaccia Research Center, via Anguillarese 301, 00123 Roma, Italy
E-mail: claudia.malerba@enea.it

Dr. C. Malerba
Department of Civil, Environental, and Mechanical Engineering University of Trento, via Mesiano 77, 38050 Trento, Italy

Dr. M. Valentini
Department of Physics University of Rome "Sapienza", P.le Aldo Moro 5, 00185 Roma, Italy

DOI: 10.1002/solr.201700101

 © 2017 WILEY-VCH Verlag GmbH & Co. KGaA, Weinheim

improvements are mainly attributed to the formation of Cu-depleted and Zn-enriched CZTSe layer near the interface with CdS.

Improvements of pure sulfide CZTS devices have been also observed after annealing of CZTS/CdS at 300 °C in N_2 atmosphere before the window layer deposition and the effect has been attributed to the improvement of the front interface quality.[15]

The study of PDA effects on kesterite solar cells has attracted further interest since an order-disorder transition was discovered both in CZTS and CZTSe compounds, with critical temperature T_c of about 270 and 200 °C, respectively.[17,4] Above this temperature, Cu and Zn cations are randomly distributed in the (Cu,Zn) (001) plane, whereas the disorder can be gradually reduced by long thermal annealing treatments below T_c (the perfectly ordered state could be reached only at $T = 0$ K) and/or by using suitable low cooling rate.[3,4,18] A very important effect of a totally disordered cation distribution is the decrease of the band gap energy E_g compared to the most ordered structure: experimentally, with the less disordered state obtained so far, the E_g variation is about 110 meV for CZTSe and 200 meV for CZTS.[3,4]

A few groups report on the influence of the ordering state of kesterite absorbers on the device performances and most of the works on this topic are addressed to selenide CZTSe or CZTSSe solar cells.

An accurate evaluation of the CZTSSe ordering effect on device parameters by Krammer and Rey shows a significant efficiency increase for ordered CZTSSe, even if the V_{oc} deficit is found not to be affected by the ordering degree of the absorber.[19,20] A similar conclusion on the V_{oc} deficit is reported in the work by Bourdais et al., in which however no efficiency change is observed.[21]

The only experimental work on this topic for pure sulfide kesterite compound is performed on CZTS monograin layer (CZTS-MGL) solar cells.[22] Optimal conditions for the ordering annealing treatment are found to be 4 h at 150 °C, leading to an increase of both V_{oc} (from 685 to 759 mV) and efficiency (from 8.1 to 9.1% on the active area), whereas similar J_{sc} and FF are found before and after the annealing. A blue shift of the CZTS PL peak of about 140 meV is observed with increasing order degree, whereas the bandgap energy, estimated from the device spectral response, seems to remain unchanged.

This work presents an investigation on the effects of the order/disorder transition in Cu_2ZnSnS_4 thin film devices. For this purpose, the absorber ordering level has been modified by PDA treatments performed on complete solar cells. Measurements on devices have been combined with direct spectrophotometric characterizations of CZTS films on glass substrates to determine the optical properties of materials with different order degree.

2. Experimental Section

2.1. Precursors Co-Sputtering Deposition

Cu-Zn-Sn-S quaternary precursors are produced by co-sputtering of three circular targets (4 inches diameter) of Cu, SnS, and ZnS (Cu: DC, 28 W; SnS: RF, 80 W; ZnS: RF, 200 W) in an Oerlikon-UNIVEX 450B sputtering system. The working pressure is 5×10^{-3} mbar with an Ar flux of 50 sccm. The precursors are deposited on soda-lime glass (SLG) and on SLG covered with 1 μm DC sputtered molybdenum, with no intentional heating of the substrates.

2.2. Sulfurization Process

CZTS film are obtained by a sulfurization treatment of precursors, performed in a new experimental system developed in collaboration with IONVAC PROCESS S.r.l. A steel vacuum chamber contains a second graphite chamber (furnace), with two graphite heaters. The precursors are loaded on a movable graphite sample holder inside the steel chamber first, and then transferred in the graphite furnace. The system is initially evacuated at a base pressure of about 10^{-1} mbar, whereas the process occurs under atmospheric pressure in nitrogen flux. Sulfur vapor is produced in a separate small graphite chamber (source) containing sulfur pellets, and then transported in the graphite furnace by a carrier gas (N_2). The source temperature (T_{S2}) can be set independently from that of the furnace, thus allowing an empirical regulation of the sulfur partial pressure (P_{S2}). In this work, all the CZTS samples are processed at 570 °C for 1 h, setting the heating ramp at 20 °C min^{-1} whereas the cooling rate is initially kept at 20 °C min^{-1} till 350 °C and then the samples are naturally cooled to room temperature in about 4 h. Sulfur vapor is produced at $T_{S2} = 230$ °C and carried into the sulfurization chamber by a 0.8 l min^{-1} nitrogen flux.

2.3. CZTS Films Characterization

The optical properties of CZTS samples grown on SLG are investigated by spectrophotometric measurements using a Perkin-Elmer LAMBDA 950 equipped with a 150 mm integrating sphere. In addition to the normal incidence transmittance (T), the complement of absorbance ($1–A = R+T$) is also measured by placing the samples inside the integrating sphere (Edwards configuration).[23] With this configuration, interference fringes are partially suppressed allowing accurate absorbance (A) measurements in the low energy region. The absorption coefficients α_T and α_A are calculated starting from T and A data, respectively, using the approximated equations:

$$\alpha_T = -\frac{1}{d}\ln\left(\frac{T}{1-R_{fa}}\right);\ \alpha_A = -\frac{1}{d}\ln\left(1-\frac{A}{1-R_{fa}}\right) \quad (1)$$

where d is the film thickness and R_{fa} is the reflectance of the film-air interface (estimated with the $1–A$ value at about 550 nm and assumed constant with λ). The effect of multiple reflection inside the film was also evaluated (using the equation reported in a previous work) and it was found to be negligible.[24] The final α spectrum of each sample is obtained by combining α_A in the low energy region with α_T in the high energy region (typically the two curves overlap in the α range 5000–1000 cm^{-1}). Finally the E_g values are derived from a linear fit of the Tauc's plot. Field Emission Scanning Electron Microscopy (SEM, Zeiss LEO 35) is

© 2017 WILEY-VCH Verlag GmbH & Co. KGaA, Weinheim

used for morphological characterization of CZTS films. Energy dispersive X-Ray spectroscopy measurements (Oxford EDX detector) are performed to check the chemical composition of the specimen. All the samples have a composition within the range $[Cu]/[Zn+Sn] \approx 0.80 \pm 0.05$ and $[Zn]/[Sn] \approx 1.25 \pm 0.05$.

2.4. Solar Cells Fabrication

CZTS based devices are completed by chemical-bath deposition of a CdS buffer layer (70 nm), followed by the sputtering deposition of intrinsic ZnO layer (50 nm, RF sputtering) and a final Transparent Conductive Oxide (TCO) of Al:ZnO (500 nm, DC sputtering) or ITO (300 nm, DC sputtering). The latter shows the same sheet resistance (about $18\,\Omega\,sq^{-1}$) but a higher transmittance (≈82% in the visible energy range) and better thermal stability than the former. The TCO deposition is made in a KENOSISTEC sputtering system on substrates heated to about 180 °C. The specimen are then naturally cooled to room temperature in few hours. For some devices (specified in the text) an additional MgF_2 anti-reflective (AR) coating (90 nm thick) is deposited by electron-beam evaporation. The active area of 0.1 cm^2 is defined by mechanical scribing.

2.5. High Temperature and Low Temperature PDA

Post Deposition Annealing treatments are performed on complete devices using two different set of conditions (temperature, dwell time, cooling rate) in order to modify the cation-ordering state in the CZTS absorber layer. As-produced (AP) devices are processed with a High Temperature PDA (HT-PDA) treatment at 300 °C (i.e., beyond T_c) on a hot-plate in air for 15 min and then cooled in few seconds on a cold metallic plate to produce a material with a high disorder degree. Low Temperature PDA (LT-PDA) is performed at 160 °C (i.e., below T_c) to increase the ordering level in the absorber layer. Due to the low kinetics of the ordering process at this temperature, the samples are annealed for at least 24 h and then slowly cooled to room temperature with rate of about 1–2 °C h^{-1}.[3] To avoid prolonged oxygen exposure at 160 °C of the solar cells, the ordering treatments are performed in a tubular furnace under N_2 atmosphere. Bare CZTS layers deposited on glass substrates undergo PDA processes similar to those used for devices, except for the use of N_2 atmosphere (instead of air) for both the ordering and disordering treatments, not to damage the absorber by direct exposure to oxygen. TCO/glass and TCO/CdS/glass samples (produced in parallel with devices) are also treated with the same HT-PDA for the optical characterization before and after the heat treatment at 300 °C.

2.6. Device Characterization

The solar cells are characterized by current voltage (J–V) measurements under dark and AM1.5 light conditions (using a WACOM WXS-140S-10 class A solar simulator) and External Quantum Efficiency (EQE) measurements.

Capacitance measurements are also performed at room temperature with an Agilent 4294A LCR/Impedance Analyzer using a 10KHz probe signal. Photoluminescence (PL) spectra are measured at 10 K in the 750 ÷ 1400 nm wavelength range on complete devices after HT-PDA and LT-PDA, using a 10 mW laser beam ($\lambda = 532$ nm).

3. Results and Discussion

3.1. Effect of PDA on CZTS Solar Cells

A significant variation of CZTS solar cells behavior has been observed after the HT and LT-PDA treatments of complete devices. The J–V curves of a typical CZTS-SC measured in the as-produced (AP) state and after the two different PDA under AM1.5 light and dark conditions are reported in **Figure 1**a and b.

Compared to the AP solar cells, a systematic improvement of the device performances is promptly observed after HT-PDA at 300 °C: indeed, despite a small reduction of the V_{oc}, both J_{sc}, and FF increase giving a significant improvement of PV conversion efficiency. In addition, the HT-PDA devices show a significant improvement of the dark J–V characteristic with reverse saturation current densities J_0 which in some cases become as low as $5.4 \cdot 10^{-9}\,A\,cm^{-2}$ and ideality factors n in the range 1.8–2.4.

The subsequent LT-PDA at 160 °C recover the V_{oc} value, but reduces the FF and J_{sc} leading to less efficient devices, which become similar to the as-produced cells.

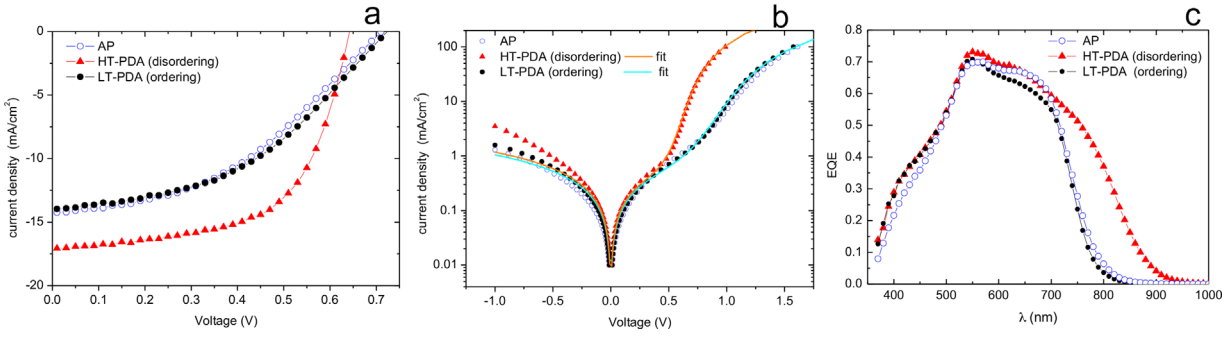

Figure 1. J–V curves of a CZTS solar cell (KC363) measured after HT and LT-PDA under AM1.5 light (a) and dark (b) conditions. In the panel c, the EQE spectra of another device (KC357) in the AP, HT-PDA and LT-PDA states are reported.

© 2017 WILEY-VCH Verlag GmbH & Co. KGaA, Weinheim

This study has been performed on some tens of solar cells, all confirming the observed trend. Some representative results are shown as examples in **Table 1**, which reports the SCs parameters after HT and LT thermal treatments.

The J_{sc} variation induced by different PDA can be ascribed to the E_g changes expected in the CZTS absorber layer due to the order/disorder transition. This is also consistent with the changes observed in the EQE spectra after different thermal treatments as reported in Figure 1c. Indeed, compared to the ordered devices, a broader EQE spectra is observed after HT-PDA, compatible with a shrinkage of the CZTS E_g upon disordering. These changes of the EQE in the spectral region $\lambda > 500$ nm are reversible (as verified repeating twice HT and LT-PDA on the same device) as the ordering state of CZTS can be reversibly modified by thermal treatments.

In addition to the reversible changes in the EQE spectrum edge related to the bandgap energy variations, it can be seen that, compared to the AP curve, a slight and permanent increase of the spectral response is observed in the low wavelength region ($\lambda < 500$) after the first HT-PDA treatment, suggesting an improvement either of the TCO front contact or of the CdS/CZTS front interface, which is preserved even after the subsequent thermal treatments (LT-PDA). A similar improvement of the EQE at low wavelength after air-annealing at 200 °C has been also reported in the literature.[13] Spectrophotometric measurements performed on both TCO/glass and TCO/CdS/glass samples (processed in parallel with the devices) confirmed an increase of the front contact transparency (about 4% in the visible energy range) after the HT-PDA, in accordance with other works.[25] In addition to this effect, the improvement of CdS/CZTS interface after thermal annealing of SCs could also be possible due to the formation of a heterophase epitaxial junction or to metals interdiffusion.[15,13]

The similarity between the AP and LT-PDA devices (see *J–V* and EQE curves in Figure 1) suggests that the thermal treatments involved in the devices fabrication (sulfurization and TCO deposition) induce a high-ordering level in the as-produced absorber layer, giving an E_g very similar to that found in the same materials after the LT-PDA.

A comparison between the *J–V* characteristics measured at different states of devices requires a particular attention because of aging-effects observed in our SCs. Indeed, whatever the state of the device (AP or HT/LT-PDA) an increase of the efficiency and in particular of the FF, is observed as the time elapsed from the last thermal treatment increases. The time scale to observe this improvement ranges from few days to some months. We point out that the effect of the different PDA on CZTS devices is immediate and much more significant if compared to the variation due to the device aging. The data reported previously in Table 1 and Figure 1 are the best results available for each SC (i.e., obtained after the device aging) measured in the HT and LT post annealed states.

It is worth noting that this aging effect does not induce any change in the shape of the EQE spectra of the cells. The effect on the *J–V* curves is instead reported in **Figure 2** for two devices with different order degree of the absorber layer measured at different aging states (d0,. . ..dn indicates the days elapsed after the PDA treatment).

The *J–V* curves of devices soon after HT-PDA (Figure 2a) exhibit a regular shape (with FF ≈ 55%) and the changes with aging are mainly due to a reduction of the series resistance leading to an improved FF (up to 64%). Similar, but more remarkable variations of the *J–V* curves with aging are observed on ordered samples (Figure 2b), with FF varying from values close to 25% (just after LT-PDA) up to over 40%. Even in this case, the similarity between *J–V* characteristics in the states LT-PDA (d0) and AP(d0) confirms the high order degree of the as-grown materials. However, FF values even lower than 25% can be found in the first few days after the ordering treatment. In particular the light *J–V* characteristics exhibit a "S-shaped" kink revealing a blocking behavior. As shown in Figure 2c, this effect is more evident just after the LT-PDA while the curves become more regular on a timescale of several days or weeks. Similar "S-shaped" light *J–V* characteristics are sometimes observed also on CIGS and CZTSe solar cells under red light illumination (the "red-kink" effect), but in our experiments this *J–V* distortion is observed even under standard AM1.5 illumination.[26–28] The mechanisms behind this effect will be discussed later. In Figure 2c, it can be also seen a cross-over between dark and light *J–V* curves, which is observed in all devices (whatever the

Table 1. Solar cell parameters of CZTS devices after different PDA treatments. The dark parameters are obtained by fitting the dark *J–V* characteristic with the standard diode equation.

Device	TCO	State	V_{OC} (mV)	J_{SC} (mA cm^{-2})	FF (%)	Eff (%)	J_0 (A cm^{-2})	n	Rs (Ω cm^2)
KC357	Al:ZnO	HT-PDA	649	19.00	56.9	7.01	1.7 E-7	2.4	3.5
		LT-PDA	658	15.09	29.1	2.89	2.9 E-6	7.8	6.0
KC363	Al:ZnO	HT-PDA	642	17.08	60.1	6.60	5.9 E-8	2.1	2.0
		LT-PDA	732	14.50	44.1	4.68	2.4 E-6	4.2	2.5
KC397	Al:ZnO + AR	HT-PDA	636	20.44	55.1	7.17	5.4 E-9	1.8	3.5
		LT-PDA	715	15.14	41.8	4.52	1.7 E-7	3.1	4.5
KC400	ITO + AR	HT-PDA	642	19.30	64.0	7.94	1.0 E-8	1.8	2
		LT-PDA	702	16.3	43.1	4.94	6.9 E-6	6.1	3
KC401	ITO + AR	HT-PDA	644	19.34	60.7	7.56	1.0 E-7	2.3	2.0
		LT-PDA	725	15.50	34.7	3.90	4.5 E-7	4.2	3.0

© 2017 WILEY-VCH Verlag GmbH & Co. KGaA, Weinheim

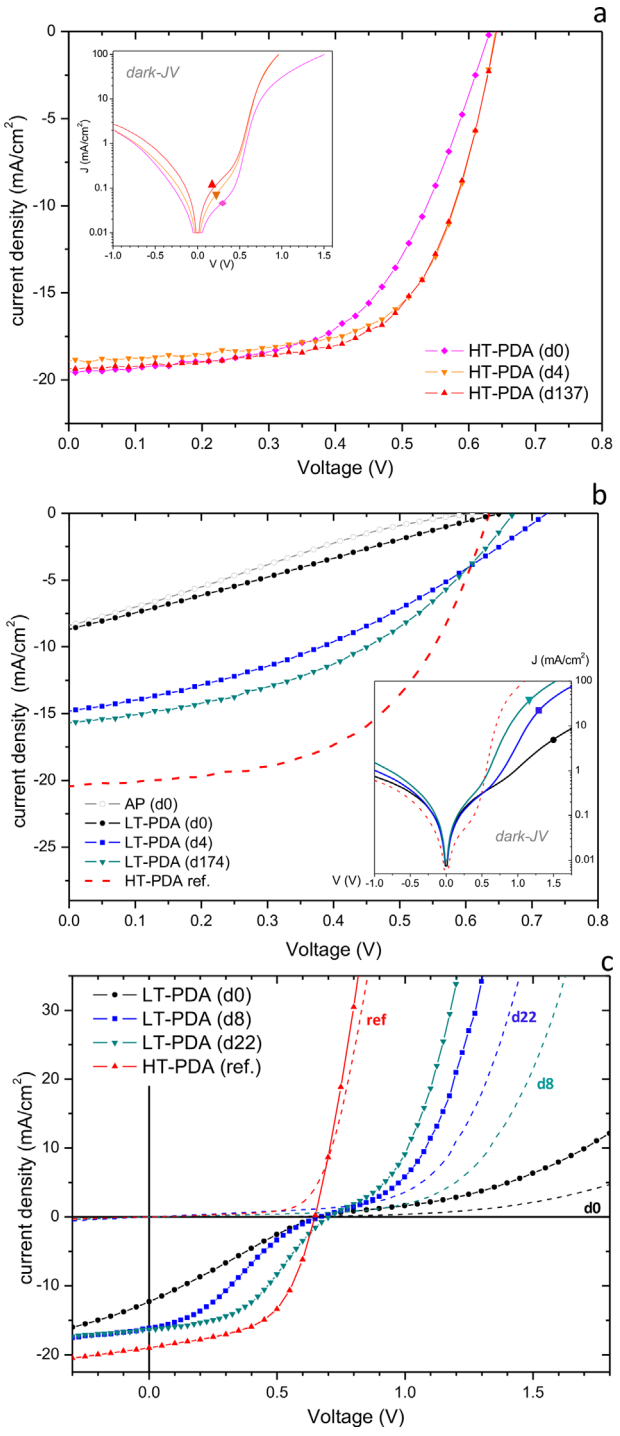

Figure 2. Aging effect on *J–V* curves of CZTS devices in the HT-PDA (panel a, KC400) and LT-PDA (panel b, KC397) states: d0,. . ..dn indicates the days elapsed after each PDA treatment. The panel c shows the S-shaped light *J–V* curves of ordered devices and the cross-over between dark (dashed lines) and light *J–V* (lines + symbols) characteristics.

order degree of the absorber) as a result of changes in the electric field distribution and recombination mechanisms under illumination. This effect is particularly significant in the ordered cells, due to the distortion of the light *JV* curve.

3.2. Effect of PDA on the Absorber Optical Properties

To investigate the correlation between the changes in SCs behavior induced by PDA and the Eg variation of CZTS related to the order-disorder transition, the optical properties of the absorber layer have been studied. Spectrophotometric measurements have been performed on CZTS samples deposited on glass substrates (produced in parallel with CZTS/Mo absorbers employed for devices) after the same LT and HT-PDA treatments used for SCs. The results show that after LT-PDA (ordering) the samples show a band gap energy which is about 170 meV higher than that found after the HT-PDA (disordering). The E_g values estimated from the plot of $(\alpha E)^2$ versus E (Tauc's plot) in **Figure 3**a for the ordered and disordered CZTS are about 1.67 and 1.50 eV, respectively, in accordance with a previous work.[3] These estimates have an uncertainty arising from the choice of the energy region used for the linear fit since, as discussed in a previous work, in polycrystalline thin films an energy region with a linear behavior of $(\alpha E)^2$ is often difficult to be univocally identified (due for example to the combined effect of interference and sub-bandgap absorption).[24] In our experiments, the error associated to E_g has been evaluated by performing the analysis in three different energy regions (shown in Figure 3a) and it is estimated to be about 20 meV.

The Urbach tails of the absorption spectra $\alpha(E)$ of ordered and disordered films derived from spectrophotometric measurements are shown in Figure 3b. A characteristic energy $\left(E_U^{\alpha}\right)$ of about 77 ± 4 meV is found for disordered samples, whereas it seems to be slightly lower for ordered film, with E_U^{α} between 64 and 73 meV (in this last case the Urbach tail cannot be accurately determined because of the more pronounced interference fringes in the α spectrum in the sub-bandgap energy region). Despite the similarity in the bandgap tails, a slight increase of the sub-bandgap absorption is observed in the disordered film, thus suggesting an increase of the deep defect density. In the same graph (Figure 3b), the Urbach tails are compared with the exponential tails observed in the EQE curves at high wavelength. The EQE tail characteristic energy $\left(E_U^{EQE}\right)$ is found to be about 45 meV, quite similar for both HT and LT-PDA devices. The difference between E_U^{α} and E_U^{EQE} is probably due to the optical absorption by deep states which do not contribute to the photocurrent. In principle, small differences in the optical properties of the CZTS/Mo layers compared to those of CZTS/SLG samples cannot be excluded, due to possible differences in materials grown on different substrates. However, the photoluminescence measurements performed on complete devices suggest that CZTS/Mo absorbers exhibit an optical behavior similar to that of CZTS/SLG samples. Indeed, as reported in Figure 3a, the PL spectra of solar cells in different ordering states show a shift of the CZTS-PL peak of about 180 meV with increasing disorder, only 10 meV higher than the E_g shift revealed in CZTS/SLG films. This result confirms that E_g changes in the same way in both CZTS/Mo and CZTS/SLG samples since the red-shift of the PL emission compared to the bandgap determined from spectrophotometry is almost independent of the ordering level of the absorber, as reported in the literature for CZTS, CZTSe, and CZTSSe compounds.[3,20,21]

© 2017 WILEY-VCH Verlag GmbH & Co. KGaA, Weinheim

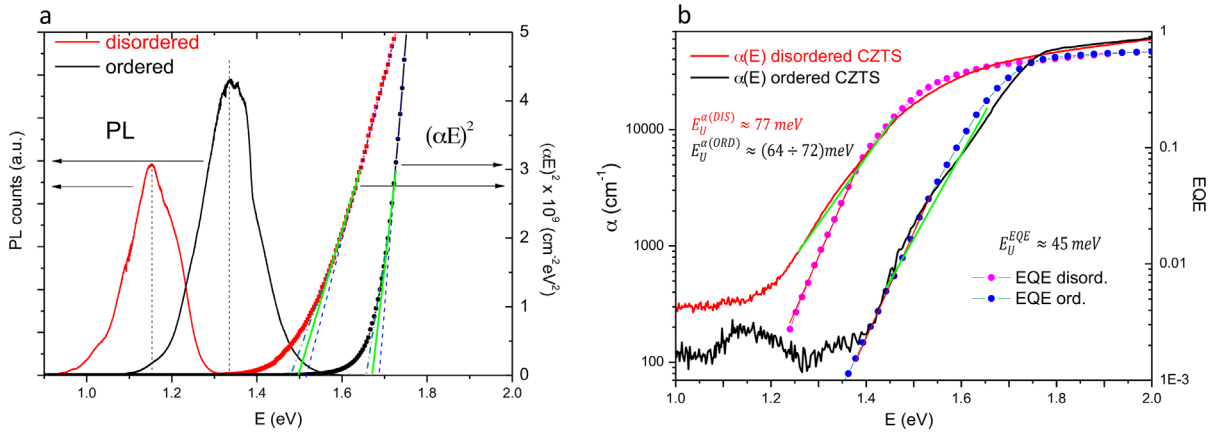

Figure 3. Panel a: Tauc's plot of a CZTS/glass sample and CZTS-PL spectra of the corresponding device in different ordering states: after HT-PDA (disordered) and LT-PDA (ordered). Panel b: comparison between the absorption spectra and EQE tails measured on the same CZTS/glass sample and solar cell.

The PL peak integral of the ordered sample is about a factor of 2 higher than that measured in disordered film, thus suggesting an increase of radiative recombination phenomena. This agrees with the decrease of the deep defect density in the ordered materials revealed by the $\alpha(E)$ spectra shown in Figure 3b. A similar increase (of about a factor 3x) of radiative recombination in ordered CZTSe samples has been also revealed by cathodoluminescence measurements as reported by Bourdais et al.[21]

A shift of the PL-peak of about 140 meV has been also observed in CZTS monograin layers (CZTS-MGL) with different ordering level.[22] However, contrary to our results, a constant value of the bandgap energy is found independently of the ordering state of the film. This could be due to the large differences in the nature of the CZTS absorbers (polycrystalline or monograin films), in the growth and post annealing conditions, but also to different methods used to estimate E_g, based on spectrophotometry in the present work and on EQE data analysis in the work by Timmo et al.[22]

Methods based on EQE data analysis are often used in the literature to estimate the bandgap energy of the absorber layer.[29] However, the EQE curve is related to the measured current (i.e., depends on free carrier generation and collection) whereas the absorption coefficient (and therefore E_g) is related to the light-absorption events only. Therefore, particular attention is required to estimate E_g from EQE data alone because the EQE shape is also influenced by the diffusion length L_n and by the space charge region width (W). For example, the method based on the Tauc's plot using $(E\ \ln(1-EQE))^2$ data versus E works under the approximation $\alpha L_n << 1$.[29,30] The use of $(E\ EQE)^2$ data versus E requires even the additional restriction $\alpha W << 1$. In poor quality devices, with small active region, these approximations are verified in an energy region close to E_g and sufficiently large to allow a proper analysis. However, in good devices with wider L_n (and/or W), these approximations are verified only in a much narrower energy region below E_g (where tail absorption dominates), thus giving an underestimated E_g value. For example, an increase of L_n in ordered CZTS layers could mask the bandgap increase compared to disordered materials. Therefore we can argue that measurements on solar cells combined with a direct optical characterization of the corresponding CZTS absorber are required to avoid possible errors in the bandgap energy evaluation and to ensure a proper investigation of the effect of the order degree on the device performances.

3.3. Analysis of the Spectral Response

In **Figure 4** the EQE spectra of a typical CZTS-SC after HT and LT-PDA are compared with the absorbance spectra (A(λ)) (corrected for the transmittance of the front contact, $T^f(\lambda)$) of the corresponding CZTS absorber in the same state. In both cases $A(\lambda)T^f(\lambda)$ (representing the ideal EQE of a device with a perfect charge collection) is much wider than the real EQE

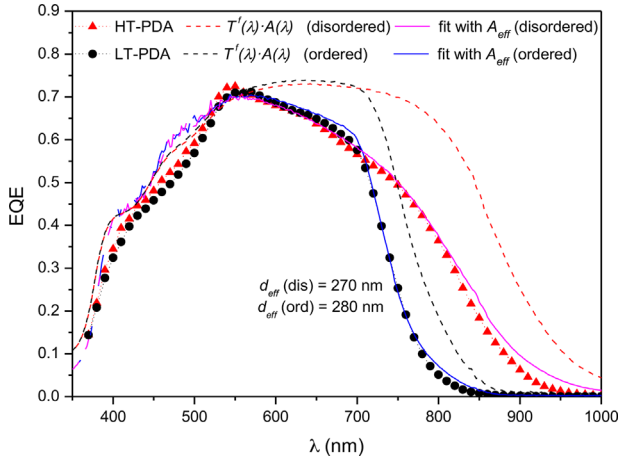

Figure 4. Comparison of experimental data and simulations of the EQE spectra of a CZTS-SC (KC397) in the HT and LT-PDA states using the effective absorbance A_{eff} as described in the text. The corrected absorbance spectra $A(\lambda)T^f(\lambda)$ of the corresponding CZTS absorber layer are also reported as EQE reference curves of an ideal device with a perfect charge collection.

© 2017 WILEY-VCH Verlag GmbH & Co. KGaA, Weinheim

spectrum, revealing that the active region of the cell is thinner than the absorber thickness.

A simple analysis of the EQE can be made by calculating an effective absorbance A_{eff} using the measured absorption coefficient α and an effective thickness d_{eff}:

$$A_{\text{eff}} = T^f(\lambda)[1 - \exp(-\alpha d_{\text{eff}})] \quad (2)$$

where $T^f(\lambda)$ is measured on a glass/CdS/IZO/AZO structure deposited in parallel with the device. To obtain a $T^f(\lambda)$ curve with no (or reduced) interference fringes, the transmittance was calculated by measuring the complement of the absorbance ($1–A = R+T$) in the Edward configuration and subtracting the reflectance of the front interface.

For all devices presented in this work, a good interpolation of the EQE experimental data are obtained using an effective thickness d_{eff} of about 270–280 nm. An example is reported Figure 4.

A more detailed analysis can be made using the approximated expression of the EQE which takes into account that the collection of photogenerated carriers is complete inside the space charge region (SCR) and limited by diffusion in the quasi neutral region:[31]

$$EQE(\lambda) = T(\lambda)\left[1 - \frac{\exp(-\alpha W)}{1 + \alpha L_n}\right] \quad (3)$$

where α is the absorption coefficient, W is the SCR width, L_n is the electron diffusion length. This expression is valid if the absorber thickness is much larger than both W and L_n. The minority carrier diffusion length can be extrapolated by a linear fit of the EQE tail with the following expression, obtained from Eq. (3) for $aW << 1$:

$$\frac{T^f(\lambda)}{\text{EQE}(\lambda)} \approx \left[\frac{1}{\alpha(L_n + W)} + \frac{L_n}{L_n + W}\right] \quad (4)$$

For all the analyzed devices, L_n is found to be about 190 nm in ordered CZTS absorber layers, whereas it is slightly lower, about 150 nm, for disordered CZTS films (see **Figure 5**). With this first estimate of L_n values, the EQE curves fits (Eq. (3)) were performed using W as the main fitting parameter. A typical analysis is shown in Figure 5 for the device KC397 (similar results were found for the other SCs).

These analyses show that in both HT and LT-PDA devices, the SCR extends for about 130 nm inside the CZTS. Using the previous estimate of L_n, the active region ($W + L_n$) of the ordered and disordered cells is about 320 and 280 nm, respectively (in accordance with the previous estimate of the effective thickness d_{eff}). We point out that the W and L_n parameters are obviously correlated and an uncertainty of about 30–40 nm can be reasonably associated to their estimates. An additional estimate of the SCR width is obtained from capacitance (C) measurements at zero bias. In disordered devices $C(V=0)$ is about 40 nF cm^{-2} and using a relative permittivity $\varepsilon_r = 6.7$ for the CZTS we obtain a SCR width of about 150 nm, in agreement with the EQE analysis within the errors.[35] The analysis of capacitance measured after the ordering treatment is more complicated due to the anomalous behavior of ordered devices, as revealed by the blocking behavior observed in the J–V curves. For example, in just ordered devices with S-shaped J–V characteristic the capacitance can fall down to 10 nF cm^{-2}, but higher capacitance values, up to about 33 nF, are measured after the device aging. This value correspond to a W of about 180 nm, slightly higher than that found from the EQE analysis. The changes in the device capacitance take place on the same time scale of those

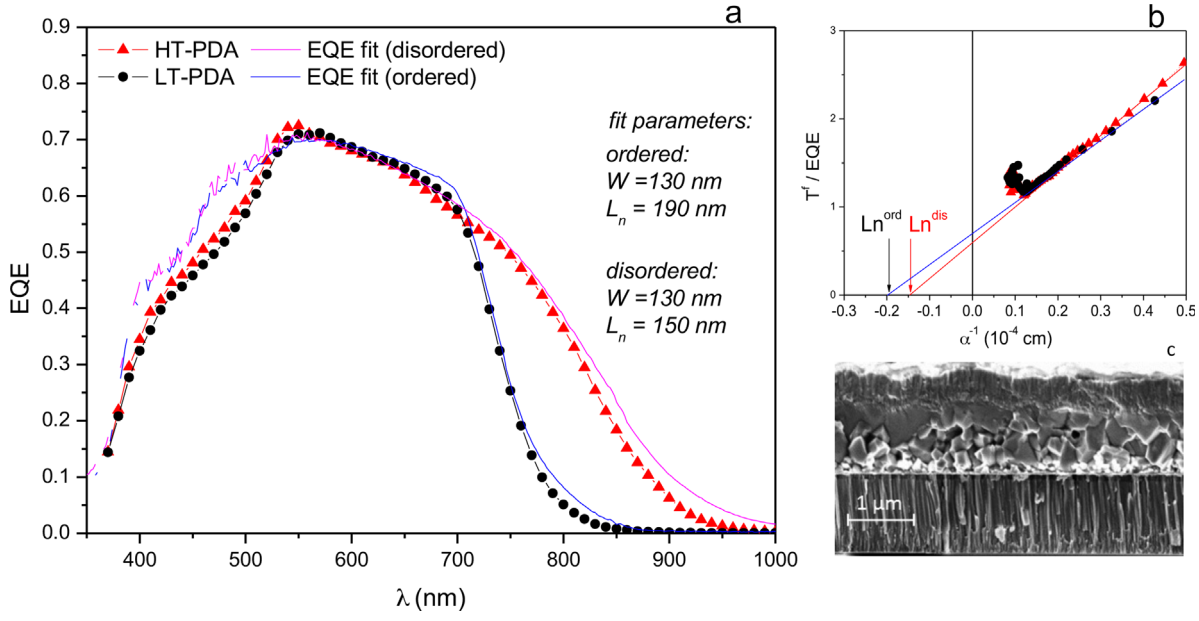

Figure 5. Fit of the EQE curves of the device KC397 with ordered and disordered CZTS absorber, analyzed with Eq. (3) (panel a). Extrapolation of L_n from the linear fit of T^f/EQE (Eq. (4)) (panel b). SEM cross section of a typical CZTS device (panel c).

© 2017 WILEY-VCH Verlag GmbH & Co. KGaA, Weinheim

observed for the J–V curves and will be discussed in the next paragraph.

Despite the uncertainty on the W and L_n estimates, the results of these EQE analysis demonstrate that the current devices are limited by a poor charge collection. The reduction of L_n (or d_{eff}) after HT-PDA could be attributed either to the increase of recombination phenomena (i.e., decrease of lifetime) and/or to a mobility decrease with increasing disorder. However, even in the case of ordered CZTS absorber layer, the L_n value is quite low compared to the typical values of high performance CZTSe devices ($L_n > 1\,\mu m$), thus revealing that the absorber quality requires further optimization.[20,32] It is worth noting that, compared to CZTSSe, the diffusion length reported for pure sulfide CZTS solar cells is usually small even for high efficiency devices: a value of about 350 nm is reported by the IBM research group for a 8.4% efficient cell and a similar value (of about 270 nm) is found by Just et al.[33,34] In our devices, the low value of L_n could be also partially due to the small grain size, as shown by the SEM cross section image (Figure 5c) of a typical solar cell obtained with the sulfurization process used in this work.

3.4. Analysis of Blocking Behavior in J–V Curves

The improvement in the performances of our devices with increasing disorder is somewhat surprising since the same type of experiments performed on CZTSSe solar cells and on CZTS monograin solar cells give the opposite result.[19,20,22]

While the J_{sc} decrease in ordered devices has been easily explained in the previous paragraph by the E_g increase, the degradation of FF and of the dark J–V curve is more difficult to be explained. We have seen that the low FF values in ordered devices are connected to a distortion of the light J–V curves which in the most severe cases are clearly S-shaped. This behavior is sometimes observed in CIGS and CZTSSe solar cells under red light illumination and three explanations have been proposed to explain it.[26–28]

As first one, the S-Shape is attributed to a spike-like conduction band alignment at the buffer/absorber interface, as in CdS/CIGS, CdS/CZTSe heterojunction or in large-gap-ZTO/CZTS solar cells.[26,28,36]

However, from XPS measurements performed on CdS/CZTS samples, a cliff alignment is reasonably expected in our devices.[37,38] Moreover, if the blocking barrier effect observed in our devices were due to a spike between CZTS and CdS, the blocking behavior would be reduced or at least unchanged after the ordering treatment, in contrast with the experimental results.

A second explanation suggests the presence in the absorber region near the CdS of a thin layer containing a large acceptor concentration.[39,40] The negative charge contained in this p^+ layer produces a large potential drop and therefore decreases the electric field in the remaining part of the absorber, consequently decreasing the FF also. If the acceptor density is high enough and when the applied bias approaches the V_{oc}, the potential in the p^+ layer will form a barrier for the electron collection reducing the photocurrent. For biases larger than the V_{oc} this barrier will disappear and the J–V curve will recover its exponential increase. This mechanisms could therefore explain the "S-shaped" light J–V. It has been argued that the p^+ layer is not a specific defected part of the absorber but arises spontaneously from the relaxation of particular compensating donors (V_{Se} or In_{Cu} in CIGS) toward a neutral charge state induced by the rise of the Fermi level near the interface.[41–43] An interesting feature of this model is that the slow relaxation of the defects could account for the aging effect observed in our devices. However, it is in contrast with our capacitance measurements, since a large capacitance value is predicted for ordered devices with S-shaped J–V, which instead show a C value lower than disordered cells with "regular" J–V. Moreover numerical simulations of devices containing a p^+ layer do indeed produce "S-Shaped" Light J–V curves but the upper inflection point is reached for a voltage lower than V_{oc}.[43,44]

Some preliminary simulations performed by us using SCAPS 3.3.02 give the same unsatisfactory results: upper flex at $V < V_{oc}$, large capacitance values and also dark J–V curves which quickly increase with bias while the experimental data show a more gradual increase of the dark current.[45] Obviously we do not claim a complete exploration of the huge parameter space involved in the simulations and therefore this model remains open to further discussion.

The third model is based on the presence of second parasitic junction (with opposite polarity to the main CZTS/CdS junction) at the CZTS/MoS_2 back interface, acting as a barrier for the hole injection.[46] To explain the S-shaped J–V curves (see the example in **Figure 6**a), the back diode reverse saturation current must be much lower than the J_{sc} of the cell, thus blocking the current as soon as the bias slightly exceeds the V_{oc}. By further increasing the bias, the back diode will enter in a breakdown regime and a quick increase of the J–V curve is recovered. In the example reported in Figure 6a the J–V characteristic of the back diode has been calculated using a simple analytical expression derived for Schottky junctions taking into account tunneling effects:[47]

$$J(V_b) = -J_{0b}\exp\left(-\frac{qV_b}{n_b k_B T}\right)\left[1-\exp\left(-\frac{qV_b}{k_B T}\right)\right] \quad (5)$$

This expression gives a current density which in reverse bias does not saturate at J_{0b} but grows exponentially with an ideality factor given by $(1–1/n_b)^{-1}$. The curve in Figure 6a was calculated with $J_{0b} = 1\,mA\,cm^{-2}$ and $n_b = 1.3$.

To get a rough estimate of the barrier height (Φ_B) requested to explain our results we can use the standard formulation for the reverse saturation current of a Schottky junction:

$$J_{0b} = A\frac{m_h^*}{m_0}T^2\exp\left(-\frac{q\Phi_B}{k_B T}\right) \quad (6)$$

where $A = 120\,A\,cm^{-2}K^2$ is the Richardson constant. Using for CZTS a hole effective mass $m_h^* = 0.48\,m_0$ we find that to obtain a J_{0b} lower than $1\,mA\,cm^{-2}$ at room temperature we should have $\Phi_B > 0.58\,eV$.

To explain our experimental data, the large height of this barrier (defined as the energy difference between the hole quasi-Fermi level and the top of the CZTS valence band at the interface CZTS/MoS_2) should decrease in the disordered state. This hypothesis is in agreement with ab-initio calculations, which suggest that the CZTS E_g reduction after disordering is mainly due to an upward shift of the valence band maximum (VBM).[48]

© 2017 WILEY-VCH Verlag GmbH & Co. KGaA, Weinheim

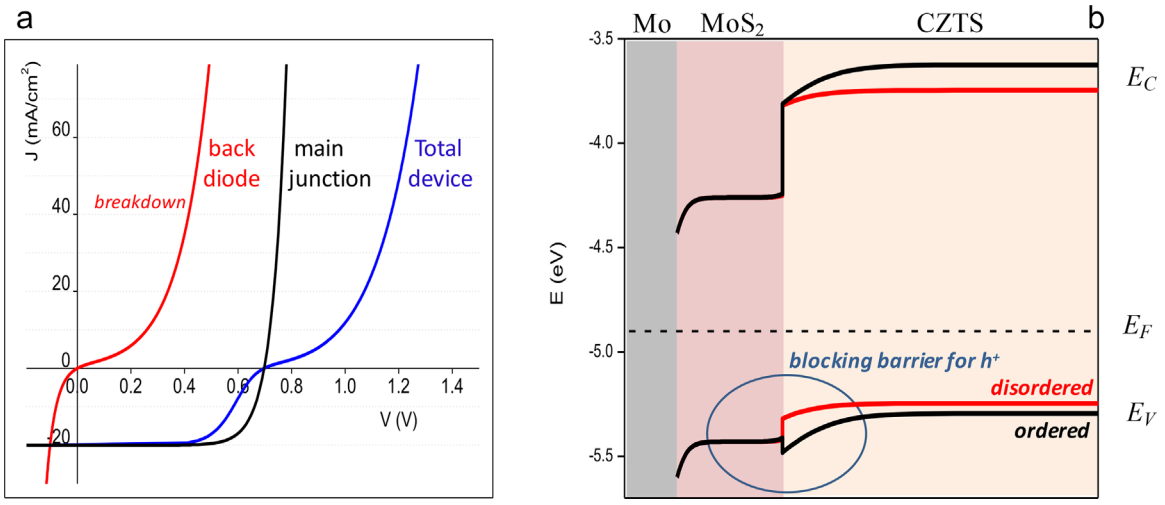

Figure 6. Panel a: back diode effect on the light *J–V* characteristic of a solar cell. The JV curves of the back (red) and front (black) junctions are reported along with the JV curve of the total device (blue). Panel b: scheme of the band profile of the Mo/MoS_2/CZTS for disordered (red line) and ordered (black line) absorber, showing a higher hole blocking barrier in ordered devices.

We can sketch the band diagram of the Mo/MoS_2/CZTS junction using the values of some relevant Mo and MoS_2 parameters collected from the literature: Mo (011) work function = 4.9 eV, $E_g(MoS_2)$ = 1.17 eV and ionization energy $E_{vac}-E_V(MoS_2)$ = 5.6 eV.[49–51] No experimental data about the valence band offset at the CZTS/MoS_2 interface are available. Since ab-initio calculations suggest that the valence band of CZTS and CIGS are aligned, we can refer to the similar case of CIG(S,Se)/Mo(S,Se)$_2$ where UPS measurements found VBM(CIGSSe) about 0.1 eV above VBM(Mo-(S,Se)$_2$).[52,53] Supposing that the same offset is present at the disordered CZTS/MoS2 interface and that the CZTS gap shift is only due to the VBM shift, we can reasonably assume a constant CZTS electron affinity = 4 eV, with $E_g(CZTS_{dis})$ = 1.5 eV and $E_g(CZTS_{ord})$ = 1.67 eV as derived from spectrophotometry measurements.

To obtain a back barrier able to explain the blocking behavior in the ordered devices (about 0.58 eV) a slightly p-type MoS_2 (E_F-E_V = 0.53 eV) has to be hypothesized (see Figure 6b). The small difference in the CZTS activation energies in Figure 6b has been just introduced to show the conductivity increase typically found in our samples in the disordered state.

Consequently, when in the disordered state, the device would have a back barrier of about 0.42 eV, which would become of about 0.58 eV after the ordering process, giving S-shaped light *J–V* curves.

From this band diagram it is clear that the quantity which critically determines the hole barrier is the Fermi level position in the MoS_2: S-shaped curves should be associated with a poorly doped MoS_2 while a high p-type doping of MoS_2 should be able to avoid any limitation to the hole injection.[54] Part of the large differences in the behavior of the cells fabricated with different procedures could therefore be due to the dependence of the MoS_2 doping on the details of the fabrication process. For example the formation of n-type MoS_2 was revealed by a XPS/UPS study performed on the Mo/MoS_2 interface produced by the sulfurization of a Mo film.[55] On the contrary, a strong p-type doping of Mo(S,Se)$_2$ was found by Kelvin probe force microscopy measurements performed on a sloped cross-section of a CZTSSe solar cell.[56]

To explain the aging effect, a change in the MoS_2 or MoS_2/CZTS interface properties should be assumed. In principle, this could be due to diffusion of atomic species (as Na or Cu) but further investigation are required to verify this hypothesis. We point out that aging effects in CIGS solar cells were observed and attributed to an increase of the back barrier.[57] Moreover, concerning the capacitance data, we point out that the back junction would introduce another space charge region in the ordered devices explaining their lower capacitance and the difference between the *W* values found from the EQE fit and the capacitance measurements.

3.5. CZTS Devices on Pre-Sulfurized Mo

The The role of the back contact on the device performances has been investigated by changing the properties of the MoS_2 layer, which usually spontaneously forms at the CZTS/Mo during the precursor sulfurization process. As discussed before, a possible reason for a bad performing back contact is a poor p-type doping of the native MoS_2 layer, which could be related to a high density of (donor-like) sulfur vacancies. A sufficient sulfur supply, therefore, could reasonably help to obtain a MoS_2 layer with proper doping and thickness, resulting in an ohmic behavior of the back contact.

To check this possibility, a sulfurization process of the Mo film has been performed before the precursor deposition to increase the sulfur content in the pre-sulfurized MoS_2 compared to the native MoS_2 layer. This route is also useful to reduce possible CZTS decomposition reaction at the CZTS/Mo interface occurring during the precursor sulfurization.[58] The sulfurization conditions used for Mo films are the same used for CZTS precursors, but the dwell time at 570 °C was reduced to 15 min. The performances of these devices are reported in **Table 2**. A standard device on not-treated Mo film is also reported in the same table for comparison.

© 2017 WILEY-VCH Verlag GmbH & Co. KGaA, Weinheim

Table 2. Solar cell parameters of CZTS devices grown on pre-sulfurized MoS_2. Different PDA treatments and aging state are specified for each device.

Device	State	Treatment	Aging (days)	V_{OC} (mV)	J_{SC} (mA cm^{-2})	FF (%)	Eff (%)	J_0 (A cm^{-2})	n	Rs (Ω cm^2)
Devices on pre-sulfurized MoS_2										
KC415	ordered	AP	0	733	13.1	54.6	5.26	1.3 E-8	2.2	5.2
	disordered	HT-PDA	0	643	15.6	52.5	5.27	4.6 E-9	2.1	5.5
	disordered	HT-PDA	108	654	16.4	56.2	6.04	3.8 E-8	2.2	3
KC444	ordered	AP	0	646	12.8	53.8	4.43	1.2 E-8	1.9	2
	ordered	AP	6	654	12.3	60.3	4.85	4.9 E-8	2.1	1.2
	ordered	AP	19	654	12.5	60.8	4.97	6.5 E-8	2.1	1.8
Ref device on standard Mo										
KC363	ordered	AP	0	697	13.4	32	2.98	1.9 E-7	3	9
	ordered	AP	75	708	14.7	44	4.57	1.7 E-7	3.2	4
	ordered	LT-PDA	150	732	14.50	44.1	4.68	2.4 E-6	4.2	2.5
	disordered	HT-PDA	0	624	17.4	54	5.89	2.5 E-7	2.45	4.5
	disordered	HT-PDA	23	642	17.08	60.1	6.60	5.9 E-8	2.09	2

The use of pre-sulfurized MoS_2 layer allows removing the blocking behavior which is instead observed in the standard solar cells (not-treated Mo) in the ordered state (AP or LT-PDA): both devices on MoS_2 in Table 2 indeed show good performances already in the AP state (corresponding to a high order degree of the absorber), with V_{oc} up to 733 mV and FF up to 60% (after aging).

The HT-PDA induces the typical V_{oc} decrease and J_{sc} increase, compatible with the bandgap energy shrinkage, whereas both FF and efficiency remain quite similar. The aging effect is still present, but the improvement of the cells with time is less remarkable compared with the standard devices because the FF of the AP SCs is already higher than 50%. These experiments are still in progress, but the optimization of the back interface using a pre-sulfurized MoS_2/Mo structure seems to be a good strategy to improve the performances of the cells produced with ordered CZTS absorber, which are obviously more attractive in view of tandem applications.

Currently, the lower efficiency of these devices compared to those on standard Mo films seems to be due to the lower J_{sc} (about 13 mA cm^{-2}), likely related to a worst morphology of the new absorbers grown on pre-sulfurized MoS_2, which often show small grain size with inhomogeneous distribution. Future work will be addressed to optimize the sulfurization conditions of precursors deposited on MoS_2 to improve the morphology of the CZTS absorber layer.

4. Conclusion

The effects of different order degree in CZTS absorber layer on solar cell performances were investigated by post deposition annealing treatments performed on complete devices. Spectrophotometric measurements revealed a bandgap energy change of about 170 meV between ordered ($E_g = 1.67$ eV) and disordered ($E_g = 1.5$ eV) CZTS films. Both the optical absorption and PL spectra suggested a higher deep defect density in disordered material, whereas the Urbach tails and the red shift of the PL peak compared to bandgap were found to be independent of the order degree. Large and reversible changes of solar-cell performances were observed after ordering/disordering treatments: photovoltaic conversion efficiencies were found to vary from about 4% for the ordered state of the absorber to nearly 8% for the disordered state. Compared to ordered devices, disordered solar cells are characterized by larger values of J_{sc} and lower V_{oc}, compatible with the CZTS E_g shrinkage induced by disordering. Ordered devices are found to be limited by low FF values, often associated with anomalous "S-shaped" light J–V curves. The worsening of ordered devices was explained by the presence of a blocking barrier for holes at the CZTS/MoS_2 back interface, arising from a poor p-type doping of the native MoS_2 layer. A route based on pre-sulfurization of molybdenum before the precursor deposition is suggested to improve the back contact behavior and therefore the performances of ordered CZTS devices.

Acknowledgments

The authors would like to thank Dr. Davide Tedeschi (Sapienza – University of Rome) for the help with the PL measurements and Enrico Salza for the skillful technical assistance. The activity is supported by the Italian Ministry of Economic Development in the framework of the Operating Agreement with ENEA for the Research on the Electric System.

Keywords

back-contact, CZTS, order-disorder, post-deposition-annealing, solar cells

Received: June 19, 2017
Revised: July 21, 2017
Published online: August 16, 2017

[1] J. Kim, H. Hiroi, T. K. Todorov, O. Gunawan, M. Kuwahara, T. Gokmen, D. Nair, M. Hopstaken, B. Shin, Y. S. Lee, W. Wang, H. Sugimoto, D. B. Mitzi, *Adv. Mater.* **2014**, *26*, 7427.
[2] W. Shockley, H. J. Queisser, *J. Appl. Phys.* **1961**, *32*, 510.

© 2017 WILEY-VCH Verlag GmbH & Co. KGaA, Weinheim

[3] M. Valentini, C. Malerba, F. Menchini, D. Tedeschi, A. Polimeni, M. Capizzi, A. Mittiga, *Appl. Phys. Lett.* **2016**, *108*, 211909.
[4] G. Rey, A. Redinger, J. Sendler, T. P. Weiss, M. Thevenin, M. Guennou, B. El Adib, S. Siebentritt, *Appl. Phys. Lett* **2014**, *105*, 112106.
[5] H. Hiroi, N. Sakai, T. Kato, H. Sugimoto, in: *Conference Record of the IEEE Photovoltaic Specialists Conference* **2013**, *863*.
[6] K. Sun, C. Yan, F. Liu, J. Huang, F. Zhou, J. A. Stride, M. Green, X. Hao, *Adv. Energy Mater.* **2016**, *6*, 1600046.
[7] A. Polizzotti, I. Repins, R. Noufi, S. H. Wei, D. Mitzi, *Energy Environ. Sci.* **2013**, *6*, 3171.
[8] A. Crovetto, O. Hansen, *Sol. Energy Mater. Sol. Cells* **2017**, *169*, 177.
[9] T. Gokmen, O. Gunawan, T. Todorov, D. Mitzi, *Appl. Phys. Lett.* **2013**, *103*, 103506.
[10] I. Repins, H. Moutinho, S. G. Choi, A. Kanevce, D. Kuciauskas, P. Dippo, C. L. Beall, J. Carapella, C. DeHart, B. Huang, S. H. Wei, *J. Appl. Phys.* **2013**, *114*, 084507.
[11] K. Sardashti, R. Haight, T. Gokmen, W. Wang, L.-Y. Chang, D. Mitzi, A. Kummel, *Adv. Energy Mater.* **2015**, *5*, 1402180.
[12] H. Xie, S. Lopez-Marino, T. Olar, Y. Sanchez, M. Neuschitzer, F. Oliva, S. Giraldo, V. Izquierdo-Roca, I. Lauermann, A. Perez-Rodriguez, E. Saucedo, *ACS Appl. Mater. Interfaces* **2016**, *8*, 5017.
[13] M. Neuschitzer, Y. Sanchez, T. Olar, T. Thersle, S. Lopez-Marino, F. Oliva, M. Espindola-Rodriguez, H. Xie, M. Placidi, V. Izquierdo-Roca, I. Lauermann, K. Leifer, A. Perez-Rodriguez, E. Saucedo, *Chem. Mater.* **2015**, *27*, 5279.
[14] D. Hironiwa, N. Sakai, T. Kato, H. Sugimoto, Z. Tang, J. Chantana, T. Minemoto, *Thin Solid Films* **2015**, *582*, 151.
[15] S. Tajima, R. Asahi, D. Isheim, D. Seidman, T. Itoh, M. Hasegawa, K. Ohishi, *Appl. Phys. Lett.* **2014**, *105*, 093901.
[16] K. Wang, O. Gunawan, T. Todorov, B. Shin, S. J. Chey, N. A. Bojarczuk, D. Mitzi, S. Guha, *Appl. Phys. Lett.* **2010**, *97*, 143508.
[17] J. J. Scragg, L. Choubrac, A. Lafond, T. Ericson, C. Platzer-Björkman, *Appl. Phys. Lett.* **2014**, *104*, 041911.
[18] K. Rudisch, Y. Ren, C. Platzer-Björkman, J. J. Scragg, *Appl. Phys. Lett.* **2016**, *108*, 231902.
[19] C. Krammer, C. Huber, T. Schnabel, C. Zimmermann, M. Lang, E. Ahlswede, H. Kalt, M. Hetterich, in *Proc. IEEE 42nd Photovoltaic Specialist Conference* **2015**, 7356096.
[20] G. Rey, T. Weiss, J. Sendler, A. Finger, C. Spindler, F. Werner, M. Melchiorre, M. Hala, M. Guennou, S. Siebentritt, *Sol. Energy Mater. Sol. Cells* **2016**, *151*, 131.
[21] S. Bourdais, C. Chonè, B. Delatouche, A. Jacob, G. Larramona, C. Moisan, A. Lafond, F. Donatini, G. Rey, S. Siebentritt, A. Walsh, G. Dennler, *Adv. Energy Mater.* **2016**, *6*, 1502276.
[22] K. Timmo, M. Kauk-Kuusik, M. Pilvet, T. Raadik, M. Altosaar, M. Danilson, M. Grossberg, J. Raudoja, K. Ernits, *Thin solid film* **2017**, *663*, 122.
[23] G. Owen, *Rev. Sci. Instrum.* **1997**, *68*, 1369.
[24] C. Malerba, F. Biccari, C. L. Azanza Ricardo, M. Valentini, R. Chierchia, M. Muller, A. Santoni, E. Esposito, P. Mangiapane, P. Scardi, A. Mittiga, *J. Alloys Compd* **2014**, *582*, 528.
[25] G. Goncalves, E. Elangovan, P. Barquinha, L. Pereira, R. Martins, E. Fortunato, *Thin Solid Films* **2007**, *515*, 8562.
[26] I. L. Eisgruber, J. Granata, J. Sites, J. Hou, J. Kessler, *Sol. Energy Mater. Sol. Cells* **1998**, *53*, 367.
[27] A. O. Pudov, J. R. Sites, M. A. Contreras, T. Nakada, H.-W. Schock, *Thin Solid Film* **2005**, *480-481*, 273.
[28] M. Neuschitzer, Y. Sanchez, S. Lopez-Marino, H. Xie, A. Fairbrother, M. Placidi, I. Haas, V. Izquierdo-Roca, A. Perez-Rodriguez, E. Saucedo, *Prog. Photovolt: Res. Appl.* **2015**, *23*, 1660.
[29] G. Zoppi, I. Forbes, R. W. Miles, P. J. Dale, J. J. Scragg, L. M. Peter, *Prog. Photovolt: Res. Appl.* **2009**, *17*, 315.
[30] C. J. Hages, N. Carter, R. Agrawal, *J. Appl. Phys.* **2016**, *119*, 014505.
[31] X. Liu, J. Sites, *J. Appl. Phys.* **1994**, *75*, 577.
[32] T. Gokmen, O. Gunawan, D. Mitzi, *J. Appl. Phys.* **2013**, *114*, 114511.
[33] B. Shin, O. Gunawan, Y. Zhu, N. A. Bojarczuk, S. J. Chey, S. Guha, *Prog. Photovolt: Res. Appl.* **2013**, *21*, 72.
[34] J. Just, M. Nichterwitz, D. Lutzenkirchen-Hecht, R. Frahm, T. Unold, *J. Appl. Phys.* **2016**, *120*, 225703.
[35] O. Gunawan, T. Gokmen, C. Warren, J. Cohen, T. Todorov, D. Barkhouse, S. Bag, J. Tang, B. Shin, D. Mitzi, *Appl. Phys. Lett.* **2012**, *100*, 253905.
[36] T. Ericson, F. Larsson, T. Torndahl, C. Frisk, J. Larsen, V. Kosyak, C. Hagglund, L. Shuyi, C. Platzer-Björkman, *Solar RRL* **2017**, *1*, 1700001.
[37] A. Santoni, F. Biccari, C. Malerba, M. Valentini, R. Chierchia, A. Mittiga, *J. Phys. D: Appl. Phys.* **2013**, *46*, 175101.
[38] C. Yan, F. Liu, N. Song, B. Ng, J. Stride, A. Tadich, X. Hao, *Appl. Phys. Lett.* **2014**, *104*, 173901.
[39] M. Topic, F. Smole, J. Furlan, *Sol. Energy Mater. Sol. Cells* **1997**, *49*, 311.
[40] A. Niemegeers, M. Burgelman, R. Herberholz, U. Rau, D. Hariskos, H.-W. Schock, *Prog. Photovolt: Res. Appl.* **1998**, *6*, 407.
[41] S. Lany, A. Zunger, *J. Appl. Phys.* **2006**, *100*, 113725.
[42] S. Lany, A. Zunger, *Phys. Rev. Lett.* **2008**, *100*, 016401.
[43] M. Igalson, A. Urbaniak, P. Zabierowski, H. Abdel Maksoud, M. Buffiere, N. Barreau, S. Spiering, *Thin Solid Films* **2013**, *535*, 302.
[44] M. Burgelman, K. Decock, S. Khelifi, A. Abass, *Thin Solid Films* **2013**, *535*, 296.
[45] M. Burgelman, P. Nollet, S. A. Degrave, *Thin Solid Films* **2000**, *361*, 527.
[46] J. Bowron, S. Damaskinos, A. Dixon, *Solar Cells* **1991**, *31*, 159.
[47] M. Missous, E. Rhoderick, *Electron. Lett.* **1986**, *22*, 477.
[48] S. Chen, A. Walsh, X. Gong, S. Wei, *Adv. Mater.* **2013**, *25*, 1522.
[49] M. Blaszczyszyn, *Surf. Sci.* **1976**, *59*, 533.
[50] W. Kautek, H. Gerischer, H. Tributsch, *J. Electrochem. Soc.* **1980**, *127*, 2471.
[51] T. Shimada, F. S. Ohuchi, B. A. Parkinson, *Jpn. J. Appl. Phys.* **1994**, *33*, 2696.
[52] S. Chen, X. G. Gong, A. Walsh, S.-H. Wei, *Phys. Rev. B* **2009**, *79*, 165211.
[53] M. Bär, S. Nishiwaki, L. Weinhardt, S. Pookpanratana, W. N. Shafarman, C. Heske, *Appl. Phys. Lett.* **2008**, *93*, 042110.
[54] F. Biccari, R. Chierchia, M. Valentini, P. Mangiapane, E. Salza, C. Malerba, C. L. Azanza Ricardo, L. Mannarino, P. Scardi, A. Mittiga, *Energy Procedia* **2011**, *10*, 187.
[55] T. Dhakal, S. Harvey, M. van Hest, G. Teeter, in *Proc. IEEE 42nd Photov. Specialist Conf. (PVSC)* 2015, https://doi.org/10.1109/PVSC.2015.7355623.
[56] K. Sardashti, E. Chagarov, P. Antunez, T. Gershon, S. Ueda, T. Gokmen, D. Bishop, R. Haight, A. Kummel, *ACS Appl. Mater. Interfaces* **2017**, *9*, 17024.
[57] T. Ott, F. Schonberger, T. Walter, D. Hariskos, O. Kiowski, R. Schaffler, *in Proc. SPIE* **2013**, *8825*, 88250J https://doi.org/10.1117/12.2024132.
[58] J. J. Scragg, T. Kubart, J. T. Wätjen, T. Ericson, M. K. Linnarsson, C. Platzer-Björkman, *Chem. Mater* **2013**, *25*, 3162.

 © 2017 WILEY-VCH Verlag GmbH & Co. KGaA, Weinheim